photonics

MDPI

Article

A Polarization-Adaptive and Multi-Wavelength-Weighted Method for Streak Image Reconstruction

Yu Zhai [1,2], Sen Xie [1,2], Wenhao Li [3], Xuan Li [1,2], Xiuli Luo [1,2], Shangwei Guo [4,5,*] and Liming Wang [1,2]

[1] State Key Laboratory of Extreme Environment Optoelectronic Dynamic Measurement Technology and Instrument, North University of China, Taiyuan 030051, China; yuzhai@nuc.edu.cn (Y.Z.); sz202405023@st.nuc.edu.cn (S.X.); lixuan@nuc.edu.cn (X.L.); lxl_tdcq@nuc.edu.cn (X.L.); wlm@nuc.edu.cn (L.W.)
[2] Shanxi Key Laboratory of Intelligent Detection Technology & Equipment, North University of China, Taiyuan 030051, China
[3] School of Electronics and Information Engineering, Suzhou Polytechnic University, Suzhou 215104, China; 92341@jssvc.edu.cn
[4] Beijing Aerospace Automatic Control Institute, Beijing 100854, China
[5] National Key Laboratory of Science and Technology on Aerospace Intelligent Control, Beijing 100854, China
* Correspondence: shwguo_12s@163.com

Abstract

To improve depth reconstruction accuracy of streak tube imaging LiDAR (STIL) under weak echo and low-contrast conditions in complex scattering environments, this paper proposes a hierarchical reliability-guided multispectral polarization reconstruction framework (MSP-STIL). The proposed method addresses measurement uncertainty in multi-wavelength and multi-polarization observations by constructing a progressive reliability modeling strategy, which evolves from polarization stability to statistical uncertainty and finally to signal strength enhancement. First, a Dual-channel Polarization Contrast (Pc) is introduced to evaluate local scattering stability and suppress fringe peak degradation caused by polarization distortion. Second, SNR is employed to model the uncertainty of depth measurements across different wavelength channels. Finally, echo intensity is incorporated as a confidence refinement factor to further enhance high-quality signals. Based on this hierarchical modeling strategy, an adaptive inverse-variance weighting scheme is developed to achieve robust multi-wavelength depth fusion. The results show that the proposed method outperforms equal-weight and single-feature methods in all test regions. Compared with the non-weighted method, the MAE, RE, MSE, RMSE, and STD are reduced by approximately 10.95%, 12.02%, 25.44%, 13.68%, and 15.58% on average, respectively. Under low signal-to-noise conditions (simulated by controlled noise levels) and long-distance detection scenarios, the proposed method still maintains low reconstruction errors and effectively suppresses depth fluctuations, demonstrating good noise resistance and distance robustness. In addition, the maximum contrast of the RGB image constructed through weighted fusion increases from 5.0065 to 5.8300, verifying the effectiveness of the proposed method in low-contrast complex scenes. Overall, the proposed MSP-STIL multi-feature joint weighting method shows clear advantages in reconstruction accuracy, robustness, and scene adaptability.

Keywords: multispectral; polarization; streak tube LiDAR; image reconstruction; adaptive fusion

Check for updates

Received: 20 May 2026
Revised: 29 June 2026
Accepted: 3 July 2026
Published: 11 September 2026

Copyright: © 2026 by the authors. Licensee MDPI, Basel, Switzerland. This article is an open access article distributed under the terms and conditions of the Creative Commons Attribution (CC BY) license.

1. Introduction

With the rapid development of three-dimensional imaging technologies in complex environment sensing, long-range target recognition, and 3D reconstruction, the ability to acquire high-resolution and multi-dimensional information has become a key direction for advanced detection systems.

Among active sensing techniques, Streak Tube Imaging LiDAR (STIL) has a unique time-to-space conversion mechanism. It maps the temporal information of echo signals into spatial positions in streak images. This enables high-precision distance measurement while simultaneously providing intensity and depth information [1–4]. Due to its high image quality, spatial resolution, range resolution, and high frame rate, STIL shows strong potential in long-range target detection applications [5–9].

However, under complex backgrounds, low-contrast conditions, and strong interference, traditional imaging methods relying only on intensity and depth information are insufficient for stable target recognition and feature extraction [10]. This limitation becomes more severe in long-distance detection and weak echo scenarios. Therefore, improving image contrast and enhancing target discriminability remains a key challenge in LiDAR systems.

To overcome these limitations, multispectral and polarization imaging techniques have been introduced into LiDAR systems to enhance feature representation and target discrimination capability [11]. Multispectral imaging captures reflectance information at different wavelengths, thereby revealing the material properties of target surfaces, while polarization imaging analyzes variations in the polarization state of echo signals to provide insights into surface geometry, roughness, and scattering characteristics. These two types of information are inherently complementary, and their integration with STIL can significantly improve imaging contrast and target discrimination performance [12].

However, the introduction of multispectral and polarization information also brings new system design challenges. In particular, under multi-wavelength and multi-polarization conditions, the fusion strategy plays a crucial role in determining imaging performance and depth accuracy. Existing studies have shown that naive or direct fusion of multi-level features may lead to information redundancy or performance degradation, highlighting the need for more effective feature grouping and fusion strategies to fully exploit complementary information [13]. Furthermore, under weak echo and noisy conditions, signal stability varies across different wavelengths and polarization channels, which increases the uncertainty of feature representation. Therefore, adaptive fusion becomes a key issue in system design.

To address these challenges, this paper focuses on collaborative enhancement of fringe reconstruction using multispectral and polarization information. Based on a multispectral polarization streak tube imaging LiDAR system (MSP-STIL), an adaptive fringe reconstruction method is proposed for complex scattering environments.

The proposed method fully exploits the complementary characteristics of spectral and polarization information. A multi-feature coupled fusion mechanism is introduced to improve peak localization stability and depth reconstruction accuracy under weak echo conditions.

Unlike conventional methods that rely on single intensity information or fixed weighting strategies, this work models the uncertainty of different observation channels under noise and scattering variations. A physically constrained adaptive weighting framework is developed.

Specifically, a Pc-based adaptive modulation mechanism is first introduced in the fringe peak reconstruction stage to improve peak stability under polarization degradation. Then, a multi-feature weighting model is constructed by integrating echo intensity, polariza-

tion stability, and peak width. This enables adaptive fusion of multi-wavelength depth information and improves ranging robustness and imaging contrast in complex environments.

The main contributions of this work are summarized as follows:

(1) An uncertainty-aware fusion framework is proposed, which formulates multi-wavelength reconstruction as an inverse-variance estimation problem under heterogeneous observation noise.
(2) A polarization-adaptive peak stabilization mechanism is developed to suppress fringe broadening under polarization degradation.
(3) A multi-feature reliability modeling strategy integrating intensity, Pc, and peak width is introduced to improve depth estimation robustness in low-SNR conditions.

Finally, simulation and experimental results validate the effectiveness of the proposed method in terms of ranging accuracy and imaging contrast enhancement.

2. Methods

To improve reconstruction accuracy and integrate multispectral and polarization information, we design a multispectral polarization streak tube imaging LiDAR system. The system collects multidimensional information via multi-wavelength emission and polarization modulation, and further improves echo information utilization efficiency by integrating an enhanced streak image reconstruction method [14]. The overall system architecture is illustrated in Figure 1.

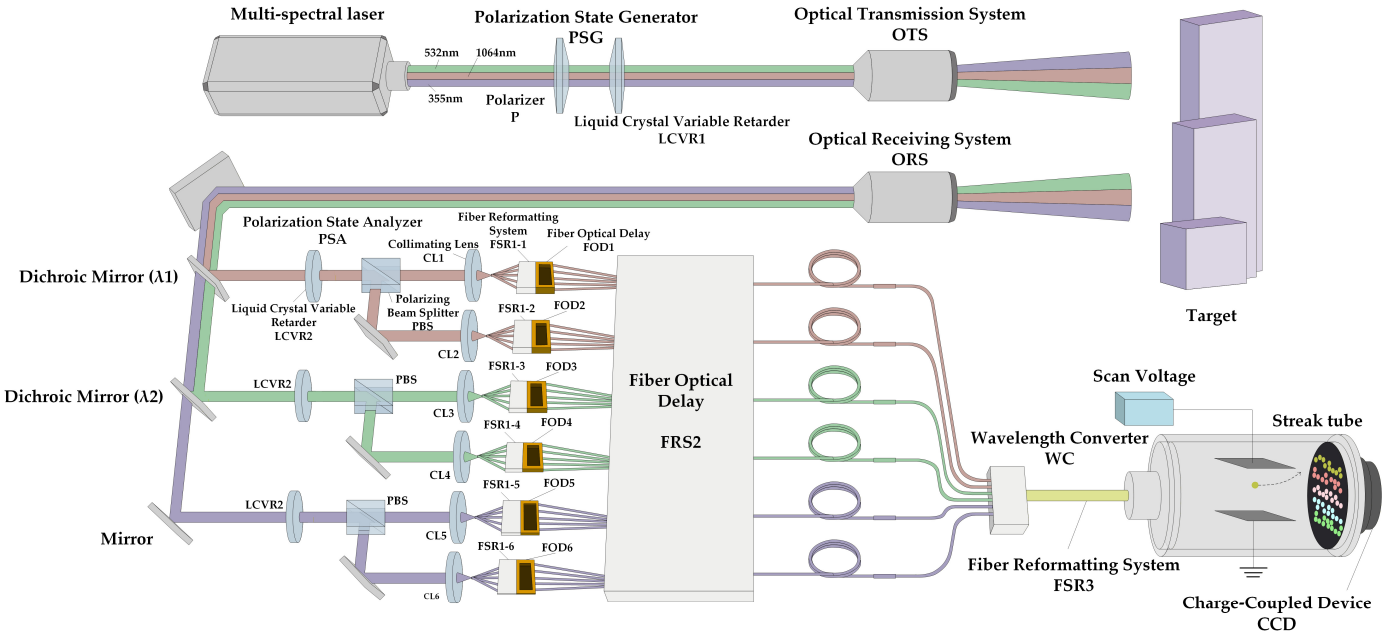


Figure 1. The schematic of MSP-STIL system.

2.1. Laser Emission System and Polarization State Modulation Mechanism

2.1.1. Multi-Wavelength Laser Emission

The system employs a multi-wavelength pulsed laser transmitter as the primary active illumination source, simultaneously emitting a composite laser beam with three specific wavelengths (λ_1, λ_2, λ_3).

The multi-wavelength design enables the acquisition of target reflection characteristics under different spectral bands, thereby providing a foundation for subsequent multidimensional information extraction.

The wavelengths of 355 nm, 532 nm, and 1064 nm are selected in this study. These wavelengths correspond to the ultraviolet, visible, and near-infrared bands, respectively.

Significant differences exist in target reflectance and atmospheric scattering characteristics across different spectral bands, which provide complementary information.

Shorter wavelengths are more sensitive to scattering variations, while longer wavelengths exhibit stronger penetration capability and better anti-interference performance. These properties help improve detection stability in complex environments.

The three wavelengths can be generated by an Nd:YAG (Neodymium-doped Yttrium Aluminum Garnet) laser through frequency conversion. This approach offers good engineering feasibility and system compatibility.

The temporal energy distribution of the emitted laser pulse approximately follows a Gaussian model, which can be expressed as follows:

$$P_t(\mathrm{t}) = \frac{E_t}{\tau\sqrt{2\pi}} \exp\left(-\frac{\mathrm{t}^2}{2\tau^2}\right) \tag{1}$$

where E_t denotes the emitted laser energy, and τ represents the pulse width.

The multi-wavelength laser beam subsequently enters the polarization modulation unit, where precise control of the polarization state of the incident light is achieved.

2.1.2. Polarization State Generation Mechanism

To obtain incident light with specific polarization characteristics, a Polarization-State Generator (PSG) is introduced at the transmitting end of the system. The module consists of a Liquid Crystal Variable Retarder (LCVR) and a Polarizer (P).

The optical axis of the LCVR forms an angle of 45° with respect to the horizontal axis, enabling adaptive modulation of the retardation under different wavelengths. The transmission axis of the polarizer is aligned parallel to the Y-axis.

Based on the Mueller matrices of the LCVR and the P, the Mueller matrix of the PSG system can be expressed as [15]:

$$M_{\mathrm{PSG}}(\delta_\lambda) = M_{\mathrm{LCVR}}(45^\circ, \delta_\lambda) M_{\mathrm{P}}(0^\circ) \tag{2}$$

and satisfies the following expression:

$$M_{\mathrm{PSG}}(\delta_\lambda) = \frac{1}{2}\begin{bmatrix} 1 & 1 & 0 & 0 \\ \cos\delta_\lambda & \cos\delta_\lambda & 0 & 0 \\ 0 & 0 & 0 & 0 \\ \sin\delta_\lambda & \sin\delta_\lambda & 0 & 0 \end{bmatrix} \tag{3}$$

Under this modulation mechanism, the incident unpolarized laser beam, represented by the normalized Stokes vector, is transformed into a laser beam with a specific polarization state. The resulting polarization-state expression is given as follows:

$$S_{t-\lambda n} = M_{\mathrm{PSG}}(\delta_{\lambda \mathrm{n}}) S_{\lambda n} = \begin{bmatrix} 1 & \cos\delta_\lambda & 0 & \sin\delta_\lambda \end{bmatrix} \tag{4}$$

The modulated laser beam subsequently enters the Optical Emission System (OES) for beam shaping and expansion, ensuring uniform and stable illumination of the target region.

2.2. Interaction Model Between Laser and Target

When the multi-wavelength polarized laser illuminates the target surface, interactions occur between the laser beam and the target surface. The intensity and polarization state of the returned signal are both affected by the reflective characteristics of the target.

The returned signal intensity satisfies the radar range equation:

$$\begin{cases} I_{irr}(t) = \frac{4\tau_a P_t(t)}{\pi(\theta_t R)^2} \\ I_{rec}(t) = I_{irr}\left(t - \frac{2R}{c}\right)\frac{\tau_a \rho(dA)}{R^2\theta_R} \\ P_{\text{det}} = I_{rec}(t)\frac{\tau_o \pi D_R^2}{4} + N_{total} \end{cases} \tag{5}$$

where θ_t denotes the divergence angle of the emitted laser beam, θ_r represents the diffuse reflection angle of the target surface, R is the distance between the detector and the target, c is the speed of light, τ_o denotes the optical transmission efficiency of the system, τ_a is the atmospheric transmittance coefficient, ρ represents the surface reflectivity of the target, D_R denotes the radius of the receiving optical lens, dA is the effective receiving area of the reflected laser signal, and N represents the noise term, including laser speckle noise, thermal noise, and background noise [16,17].

Speckle noise arises from the interference between coherent laser scattering on rough target surfaces and the detector response. It is inherently random and is typically modeled as signal-dependent multiplicative noise. Its statistical properties can be approximated by a negative binomial distribution. Background noise is mainly induced by environmental radiation, including solar illumination, ambient light, and atmospheric scattering. It generally follows a Poisson distribution. Thermal noise originates from thermal motion in the detector and electronic circuits. It is modeled as additive Gaussian white noise, whose intensity depends on circuit temperature and device parameters. In addition, dark current noise is also introduced as an additive noise component.

Based on the above model, the total number of detected photons in the system can be expressed as:

$$N_{total} = N_{signal} + N_{speckle} + N_{thermal} + N_{background} \tag{6}$$

Under a single-mode configuration (i.e., no birefringent materials in the target region), the model is simplified by assuming that the target surface can be represented using a 4×4 diagonal Mueller matrix:

$$M_\lambda = diag\begin{bmatrix} m_{00}^\lambda & m_{11}^\lambda & m_{11}^\lambda & m_{33}^\lambda \end{bmatrix} \tag{7}$$

where m_{00}^λ represents the surface reflectivity of the target, while m_{11}^λ and m_{33}^λ characterize the polarization properties of the target surface.

In this study, a diagonal Mueller matrix is adopted to simplify the modeling of polarization scattering. This assumption is valid under conditions where single scattering is dominant and depolarization effects are relatively weak. The model is mainly applicable to scenarios in which single scattering dominates, depolarization is weak, and no significant birefringent materials exist in the target region. For natural surfaces or complex artificial targets, multiple scattering and depolarization effects may introduce non-diagonal elements in the Mueller matrix, thereby affecting the accurate representation of polarization characteristics. The purpose of adopting this model is to reduce the complexity of system modeling and simulation, and to highlight the core mechanism of the proposed reconstruction method, making it suitable for simulation studies of polarization imaging LiDAR systems.

According to Equation (5), after reflection from the target surface, the polarization state of the incident laser beam becomes:

$$S_{rec-\lambda n}^{i,j} = M_{\lambda n}^{i,j} S_{irr-\lambda n}^{i,j}\left(t - \frac{2R^{i,j}}{c}\right)\frac{\tau_a \rho(dA)}{R^2\theta_R} \tag{8}$$

where $S_{irr-\lambda n}^{i,j}$ denotes the polarization state of the laser beam incident on the local target region, and $R^{i,j}$ represents the distance between the local target region and the imaging system.

2.3. Echo Signal Reception and Imaging Procedure

The core objective of the receiving process is to separate, delay, and transmit the multi-wavelength and multi-polarization echo signals reflected from the target, thereby ensuring that the signals enter the streak tube in an ordered manner to complete the imaging process.

2.3.1. Polarization and Spectral Separation

After reflection from the target surface, the multi-wavelength polarized echo signals are collected by the Optical Receiver System (ORS). The signals subsequently enter a Polarization-State Analyzer (PSA) composed of an LCVR and a Polarizing Beam Splitter (PBS).

In the PSA system, the optical axis of the LCVR forms an angle of 135° with respect to the Y-axis and generates a phase retardation of δ_n. The PBS separates the incident laser beam into the ordinary ray (o-ray) and the extraordinary ray (e-ray). Accordingly, the Mueller matrices of the PSA system can be expressed as follows:

$$\begin{cases} M_{\mathrm{PSA}-o}(\delta_\lambda) = M_{\mathrm{P}}(0^\circ) M_{\mathrm{LCVR}}(135^\circ, \delta_\lambda) \\ M_{\mathrm{PSA}-e}(\delta_\lambda) = M_{\mathrm{P}}(90^\circ) M_{\mathrm{LCVR}}(135^\circ, \delta_\lambda) \end{cases} \tag{9}$$

And satisfy the following expressions:

$$\begin{cases} M_{\mathrm{PSA}-o}(\delta_\lambda) = \frac{1}{2}\begin{bmatrix} 1 & \cos\delta_\lambda & 0 & \sin\delta_\lambda \\ 1 & \cos\delta_\lambda & 0 & \sin\delta_\lambda \\ 0 & 0 & 0 & 0 \\ 0 & 0 & 0 & 0 \end{bmatrix} \\ M_{\mathrm{PSA}-e}(\delta_\lambda) = \frac{1}{2}\begin{bmatrix} 1 & -\cos\delta_\lambda & 0 & -\sin\delta_\lambda \\ -1 & \cos\delta_\lambda & 0 & \sin\delta_\lambda \\ 0 & 0 & 0 & 0 \\ 0 & 0 & 0 & 0 \end{bmatrix} \end{cases} \tag{10}$$

The Stokes vector of the o-ray, $S_{\lambda n-o}^{i,j}(t)$, and that of the e-ray, $S_{\lambda n-e}^{i,j}(t)$, can be expressed as follows:

$$\begin{cases} S_{\lambda n-o}^{i,j}(t) = M_{\mathrm{PSA}-o}(\delta_{\lambda n}) S_{rec-\lambda n}^{i,j}(t) \\ S_{\lambda n-e}^{i,j}(t) = M_{\mathrm{PSA}-e}(\delta_{\lambda n}) S_{rec-\lambda n}^{i,j}(t) \end{cases} \tag{11}$$

where $S_{\lambda n-o}^{i,j}[t](0)$ and $S_{\lambda n-e}^{i,j}[t](0)$ denotes the first element of the Stokes vector, namely the light intensity. According to Equation (5), the powers of the o-ray and e-ray incident on the photocathode of the streak tube are $P_{\lambda n-o}^{i,j}(t)$ and $P_{\lambda n-e}^{i,j}(t)$, respectively, which can be determined as follows:

$$\begin{cases} P_{\lambda n-o}^{i,j}(t) = \frac{\tau_{\lambda n}\pi D_{\mathrm{R}}^2}{4} S_{\lambda n-o}^{i,j}(t)[0] + N_1 \\ P_{\lambda n-e}^{i,j}(t) = \frac{\tau_{\lambda n}\pi D_{\mathrm{R}}^2}{4} S_{\lambda n-e}^{i,j}(t)[0] + N_2 \end{cases} \tag{12}$$

where $\tau_{\lambda n}$ denotes the transmittance of the echo signal at wavelength λ_n within the optical system.

After polarization separation, the signals corresponding to different wavelengths and polarization states form six independent channels. Each channel is first focused by a Convergent Lens (CL) and subsequently coupled into the fiber array of the Optical Fiber

Remapping System (FRS). The echo signal of each group then undergoes temporal delay processing through the corresponding Fiber-Optic Delay (FOD), ensuring that signals from different groups enter the Wavelength Converter (WC) sequentially in time. After wavelength conversion, signals at different wavelengths are uniformly converted into laser pulses with a specific wavelength λ, and are subsequently injected into the streak tube in chronological order.

2.3.2. Streak Image Formation

The streak tube converts the input signal through an optical–electrical–optical transformation process. The luminous intensity generated by the laser pulse on the phosphor screen of the streak tube can be expressed as follows [14]:

$$I(x,y) = \tau_s \int P_t(t) G(x, y - tv_s) dt \tag{13}$$

where (x, y) denotes the spatial coordinates, τ_s is the optical-to-phosphor conversion efficiency of the streak tube, P_t represents the incident laser pulse power, $G(x, y)$ denotes the geometrical profile of the laser spot, which is approximately described by a two-dimensional Gaussian distribution, and v_s is the scanning speed of the streak tube.

For the spots corresponding to the o-ray and e-ray, the intensity model can be further expressed by combining polarization characteristics and the ranging equation as follows:

$$\begin{cases} G(x,y) = \frac{1}{4\pi\tau_1\tau_2} \exp\left(-\frac{1}{2}\left(\frac{x^2}{2\tau_1^2} + \frac{y^2}{2\tau_2^2}\right)\right) \\ E(x,y) = \exp\left(-\frac{x^2}{4\tau_1^2} - \frac{\left(y - \frac{2R^{i,j}}{c} v_s\right)^2}{4\tau_2^2 + 2\tau^2 v_s^2}\right) \\ C = \frac{E_t \tau_s \tau_{\lambda n} \tau_\alpha^2 D_R^2 \rho dA}{4\pi\theta_R \theta_t^2 \left(R^{i,j}\right)^\tau \sqrt{4\tau_2^2 + 2\tau^2 v_s^2}} \\ A_{\lambda n-o}^{i,j} = C\left(m_{00}^{\lambda n,i,j} + m_{11}^{\lambda n,i,j} \cos^2\delta_{\lambda n} + m_{33}^{\lambda n,i,j} \sin^2\delta_{\lambda n}\right) \\ B_{\lambda n-e}^{i,j} = C\left(m_{00}^{\lambda n,i,j} - m_{11}^{\lambda n,i,j} \cos^2\delta_{\lambda n} - m_{33}^{\lambda n,i,j} \sin^2\delta_{\lambda n}\right) \\ I_{\lambda n-o}^{i,j}(x,y) = \tau_s \int P_{\lambda n-o}^{i,j}(t) G(x, y - tv_s) dt = A_{\lambda n-o}^{i,j} E(x,y) \\ I_{\lambda n-e}^{i,j}(x,y) = \tau_s \int P_{\lambda n-e}^{i,j}(t) G(x, y - tv_s) dt = B_{\lambda n-e}^{i,j} E(x,y) \end{cases} \tag{14}$$

where τ_1 and τ_2 denote the spot dimensions in the x- and y-directions, respectively; C is a constant related to the system parameters. The peak position of the spot is given by $x = 0$ and $y = 2R^{i,j}v_s/c$, from which the target range can be inferred based on the peak position [18]; $I_{\lambda n-o}^{i,j}$ and $I_{\lambda n-e}^{i,j}$ represent the intensities of the spots generated by the o-ray and e-ray laser pulses with wavelength λn, respectively.

2.4. Streak Image Reconstruction

In the MSP-STIL system, after polarization analysis, the echo signal at each wavelength is decomposed into two polarization components: the ordinary ray (o-ray) and the extraordinary ray (e-ray). Consequently, the system finally acquires six streak images, corresponding to three wavelengths and two polarization-state combinations.

Each streak image consists of $N \times N$ spots, which essentially represent the spatiotemporal mapping results of the echo signals. The objective of streak image reconstruction is to accurately extract the intensity, depth, and polarization information of each spot.

At the same wavelength, the o-polarized and e-polarized components exhibit different energy distributions and polarization characteristics during target scattering and propagation. To fully exploit polarization information, an adaptive fusion model based on **Pc** is introduced in the fringe image reconstruction stage.

For the polarization images corresponding to the three wavelengths λ_1, λ_2 and λ_3, the $Pc_{\lambda n}^{i,j}$ is calculated as follows:

$$Pc_{\lambda n}^{i,j}(x,y) = \left| \frac{I_{\lambda n-o}^{i,j}(x,y) - I_{\lambda n-e}^{i,j}(x,y)}{I_{\lambda n-o}^{i,j}(x,y) + I_{\lambda n-e}^{i,j}(x,y)} \right| \tag{15}$$

where $I_{\lambda n-o}^{i,j}(x,y)$ and $I_{\lambda n-e}^{i,j}(x,y)$ denote the local echo intensities of the o-ray and e-ray components, respectively, corresponding to wavelength λ within the (i,j)-th streak unit.

When the Pc is high, it indicates a significant difference between the two orthogonal polarization components. In this case, the polarization characteristics of the echo signal are more stable, and the corresponding fringe peaks are more concentrated with clearer structures, which is beneficial for accurate peak localization.

When Pc is low, the difference between the orthogonal polarization components becomes weaker. The echo signal contains a higher proportion of random components or multipath effects, leading to peak broadening in the fringe pattern and increased uncertainty in peak localization.

Therefore, Pc can be regarded as an effective measure of polarization stability in the proposed system.

Based on these characteristics, the o-ray and e-ray streak spots are processed to obtain the reconstructed spot $I_{\lambda n}^{i,j}(x,y)(n=1,2,3)$, which can be expressed as follows:

$$I_{\lambda n}^{i,j}(x,y) = \omega_{\lambda n-o}^{i,j}(x,y) I_{\lambda n-o}^{i,j}(x,y) + \omega_{\lambda n-e}^{i,j}(x,y) I_{\lambda n-e}^{i,j}(x,y) \tag{16}$$

The weighting coefficients are determined by the local Pc.

$$\begin{cases} \omega_{\lambda n-o}^{i,j} = \frac{1+Pc_{\lambda n}^{i,j}}{2} \\ \omega_{\lambda n-e}^{i,j} = \frac{1-Pc_{\lambda n}^{i,j}}{2} \end{cases} \tag{17}$$

According to the streak spot intensity distribution expressed in Equation (14), the exponential term contains:

$$\left(y - \frac{2R^{i,j}}{c} v_s \right)^2 \tag{18}$$

When the spot intensity reaches its maximum value, the exponential term attains its minimum value, yielding:

$$y = \frac{2R^{i,j}}{c} v_s \tag{19}$$

Accordingly, the relationship between the target distance and the streak peak position can be derived as follows:

$$R^{i,j} = \frac{c}{2v_s} y \tag{20}$$

The localization accuracy of the peak position y directly determines the accuracy of range inversion. According to the error propagation theory, the ranging error can be expressed as follows:

$$\sigma_R = \left| \frac{\partial R^{i,j}}{\partial y} \right| \sigma_y = \frac{c}{2v_s} \sigma_y \tag{21}$$

where σ_y denotes the positional uncertainty of the streak peak along the scanning direction.

In the actual imaging process, the echo intensity is positively correlated with the SNR, whereas the peak width reflects the uncertainty of peak localization. Therefore, the ranging

error approximately satisfies an inverse relationship with the SNR, which influences the peak width and localization stability:

$$\sigma_R \propto \frac{1}{\mathrm{SNR}} \tag{22}$$

Meanwhile, a smaller peak width corresponds to higher ranging accuracy. Based on the above analysis, the echo intensity and peak width are employed to construct the multi-wavelength fusion weights in this study.

In this study, σ_R represents the uncertainty in the estimation of the fringe peak position. Its main sources include echo signal noise, peak broadening, and statistical fluctuations introduced by multi-wavelength fusion. According to error propagation theory, the peak localization error is inversely proportional to the SNR.

When the SNR is high, the echo peak becomes more concentrated, leading to higher peak localization accuracy and reduced distance estimation error. Conversely, under low-SNR conditions, increased noise disturbances cause peak broadening, thereby increasing σ_R.

Therefore, σ_R can be interpreted in a statistical sense as the uncertainty of distance estimation derived from peak width, which fundamentally reflects the influence of echo signal quality on ranging accuracy. Under this physical relationship, the weighting strategy proposed in this work, based on echo intensity and peak width, is essentially equivalent to an adaptive inverse-variance fusion mechanism driven by SNR.

The weighting coefficient is defined as follows:

$$\omega_{\lambda n}^{i,j} = \frac{1/\sigma_{R\lambda n}^2}{\sum_{k=1}^{3} \left(1/\sigma_{R\lambda k}^2\right)} \tag{23}$$

where σ_R represents the estimated range uncertainty derived from peak width, reflecting the stability of peak localization. This uncertainty is influenced by signal quality and is indirectly related to the SNR. σ_R represents the standard deviation of the range estimation error. In this work, it is approximated using the peak width (FWHM) of the streak signal, which is further linked to the SNR. Under Gaussian noise assumptions, the variance of the range estimation is inversely proportional to SNR. Therefore, the weighting strategy in Equation (23) can be interpreted as an inverse-variance weighted fusion scheme, where σ_R^2 approximates the variance of the range estimator. This uncertainty is influenced by signal quality and is indirectly related to the SNR.

A peak detection algorithm [19] is further employed to extract the intensity and depth information of the spot $I_{\lambda n}^{i,j}(x,y)$ $(n = 1,2,3)$. Subsequently, the intensity value $I_{\lambda n}^{i,j}$ and depth value $R_{\lambda n}^{i,j}$ of the (i,j)-th spot at wavelength λ_n are obtained.

Finally, the depth value $D^{i,j}$ of the spot at pixel (i,j) is obtained by weighted fusion of the depth $R_{\lambda n}^{i,j}(n = 1,2,3)$, intensity $I_{\lambda n}^{i,j}(n = 1,2,3)$, and parameter $\omega_{\lambda n}$ across the three wavelengths, as given by:

$$D^{i,j} = \sum_{n=1}^{3} I_{\lambda n}^{i,j} \omega_{\lambda n}^{i,j} R_{\lambda n}^{i,j} \tag{24}$$

In summary, the proposed streak image reconstruction method consists of three key stages: spot information extraction, polarization-adaptive fusion, and multi-wavelength weighted reconstruction. The method fully exploits the complementarity between multi-spectral and polarization information, enabling high-precision recovery of echo intensity and time-of-arrival information, thereby achieving the reconstruction of intensity images,

polarization images and depth images. Consequently, it provides a reliable data foundation for subsequent target recognition and precise ranging applications.

3. Experiments and Results

To ensure the physical consistency of the MSP-STIL simulation, as listed in Table 1, the system modeling comprehensively considers key factors, including laser emission characteristics, target reflection properties, and optical receiver system parameters, as well as the performance characteristics of the detector and streak tube.

Table 1. System Parameter Settings.

Parameter	Setting
Pulse energy E_t/J	1
Pulse width τ/ns	5
Operating wavelengths λ/nm	355/532/1064
Angular dispersion of target θ_r/rad	π
Angular dispersion of laser θ_t/rad	0.024
Field of view α/°	3
Focal length F/m	0.04
Receiver aperture radius D_R/m	2×10^{-3}
Optical transmittance τ_λ	0.75/0.68/0.62
Atmospheric transmittance τ_α	0.9
Conversion efficiency τ_s	1.1×10^4
Scanning speed v_s/μm · ns^{-1}	100
Number of echo signals	$6 \times 64 \times 64$
CCD resolution	4096×4096
spatial resolution SR/cm · pixel^{-1}	1.3
Frame rate f/Hz	60
Background noise N_B/W · m^{-2}	100
dark current N_d/A	1×10^{-9}

3.1. Accuracy Validation Experiment

We evaluate the reconstruction accuracy using a four-layer stepped target simulation. Materials with different spectral reflection characteristics and polarization scattering properties were selected as target surfaces. By incorporating their reflectivity parameters and Mueller matrix parameters into the LiDAR imaging model, single-wavelength depth images at the three operating wavelengths were obtained individually. We then generate the optimized depth image using the proposed fusion method.

On this basis, different fusion strategies are constructed for comparison, including equal-weight fusion, intensity-only weighting, uncertainty-only weighting, Pc-only weighting, and a method without polarization information. These methods are further compared with the proposed multi-feature joint weighting approach.

In the experiments, the MSP-STIL system is used to illuminate a trapezoidal target at a distance of 1000 m. The target consists of four stepwise layers, as shown in Figure 2. Each layer is a rectangular plane with dimensions of 4 m × 1 m, and the vertical spacing between adjacent layers is 1 m. To reflect the influence of different material properties on imaging results, the surfaces of the four layers are coated with fabric, concrete, paper, and aluminum from top to bottom, respectively.

The surface reflectance and Mueller matrix parameters of the four materials at wavelengths of 355 nm, 532 nm, and 1064 nm are listed in Table 2.

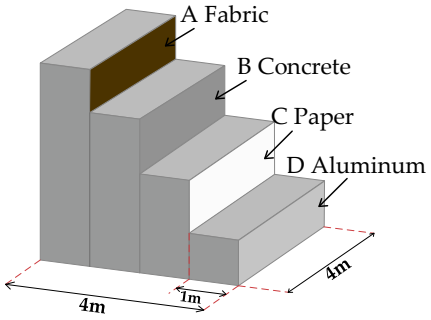


Figure 2. Stepwise Model.

Table 2. Reflectance and Polarimetric Parameters (m_{11}, m_{33}) of Different Materials at Multiple Wavelengths.

	A Fabric			**B Concrete**			**C Paper**			**D Aluminum**		
Parameter	λ_1	λ_2	λ_3	λ_1	λ_2	λ_3	λ_1	λ_2	λ_3	λ_1	λ_2	λ_3
Reflectivity	0.46	0.54	0.56	0.51	0.588	0.56	0.87	0.82	0.79	0.36	0.362	0.425
m_{11}	0.375	0.4	0.28	0.185	0.19	0.228	0.162	0.16	0.6	0.8	0.867	0.98
m_{33}	0.372	0.37	0.3	0.19	0.193	0.24	0.17	0.175	0.63	0.78	0.851	0.98

To comprehensively evaluate the depth reconstruction performance of the proposed method, several metrics are adopted, including Mean Absolute Error (MAE), Relative Error (RE), Mean Squared Error (MSE), Root Mean Square Error (RMSE), and Standard Deviation (STD).

MAE measures the average deviation between the reconstructed depth and the ground truth, providing an intuitive indication of the overall error level. RE describes the error relative to the true value, which helps analyze error distribution across different scales. MSE accumulates squared errors and is more sensitive to large deviations, thus penalizing outliers more strongly. RMSE, as the square root of MSE, shares the same physical units as the measured quantity, enabling intuitive interpretation of error magnitude. STD characterizes the dispersion of errors and is used to evaluate the stability of the method across pixels or repeated experiments.

Through this multi-metric analysis, the accuracy and stability of depth reconstruction results can be comprehensively evaluated, thereby providing an objective assessment of the advantages of the proposed method.

Theoretically, the true depth of the same target should remain consistent across different wavelengths. Therefore, the three single-wavelength depth images are expected to share an identical spatial layer structure. However, due to differences in reflectance properties and polarization scattering characteristics of various materials at different wavelengths, each step region exhibits different echo intensity, polarization response, and fringe peak structures during imaging. This leads to variations in peak localization accuracy, resulting in discrepancies in the reconstructed depth images obtained at different wavelengths.

On this basis, different fusion strategies exhibit different capabilities in suppressing these errors. Therefore, multiple weighting schemes, including equal weighting, intensity-only weighting, SNR-only weighting, polarization-only weighting, and non-polarization fusion, are constructed for comparison. The reconstruction performance of each method is evaluated across different material regions to systematically analyze the influence of each weighting factor on depth estimation accuracy.

Finally, the effectiveness and stability of different weighting strategies are quantitatively evaluated by analyzing the statistical results of reconstructed depth images in each step region and computing the Mean Squared Error (MSE) and Standard Deviation

(STD). This allows for verification of the rationality of the proposed multi-feature joint weighting method.

The parameters of the four-layer step target are then input into the multispectral polarization streak tube LiDAR imaging simulation model. Imaging is performed under three wavelengths, and three corresponding single-wavelength depth images are obtained, as shown in Figure 3.

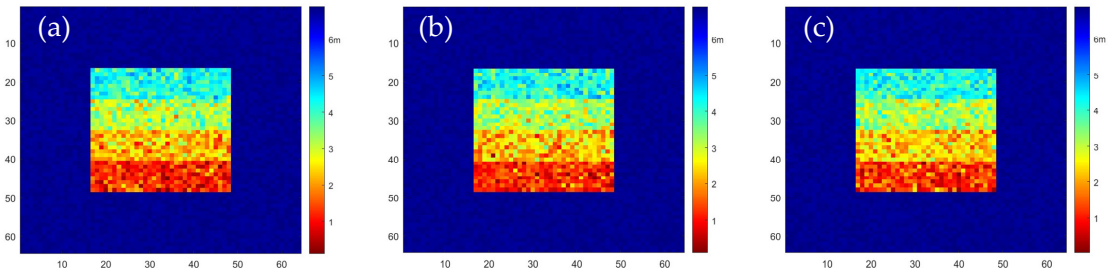


Figure 3. Step depth images at different wavelengths. (**a**) Step depth image at wavelength λ_1. (**b**) Step depth image at wavelength λ_2. (**c**) Step depth image at wavelength λ_3.

Under the condition that the experimental scenario, target parameters, and data processing pipeline remain consistent, multiple fusion strategies are designed for ablation analysis in this study.

Specifically, an equal-weight fusion method (Equal) is first introduced, which assigns identical weights to different polarization components and multi-wavelength depth results, serving as the baseline method.

Next, single-feature weighting strategies are constructed, including intensity-only weighting (I-only), uncertainty ratio weighting (uncertainty-only), and Pc weighting (Pc-only). These methods respectively use echo intensity, signal quality, and polarization stability as weighting criteria.

On this basis, dual-feature fusion strategies are further developed, including intensity and Pc (I + Pc), intensity and uncertainty (I + uncertainty), and Pc and uncertainty (Pc + uncertainty), in order to analyze the impact of different feature combinations on fusion performance.

Finally, all the above methods are used as baseline comparisons. The proposed multi-feature adaptive weighting method (I + Pc + uncertainty) jointly considers echo intensity, polarization stability, and uncertainty, while also incorporating peak width to model uncertainty. This enables a more reasonable weight allocation mechanism, thereby improving depth reconstruction accuracy and robustness.

For the above fusion strategies, three single-wavelength depth images are respectively fused to obtain multiple sets of depth reconstruction results. The reconstructed depth images obtained by different methods are shown in Figure 4. The results include comparisons under multiple fusion strategies, which provide a direct visualization of the influence of different weighting mechanisms on depth estimation performance.

After obtaining the reconstructed depth images for each method, statistical analysis is conducted on the four step regions, and the mean depth values are calculated. Evaluation metrics including MAE, RE, MSE, RMSE, and STD are further computed.

The results for regions A–D are listed in Tables 3–6.

As shown in Tables 3–6, weighting methods based on a single feature (intensity, polarization, or uncertainty) can reduce reconstruction errors to some extent. However, their performance varies significantly across different regions, indicating that a single feature is insufficient to fully characterize ranging reliability.

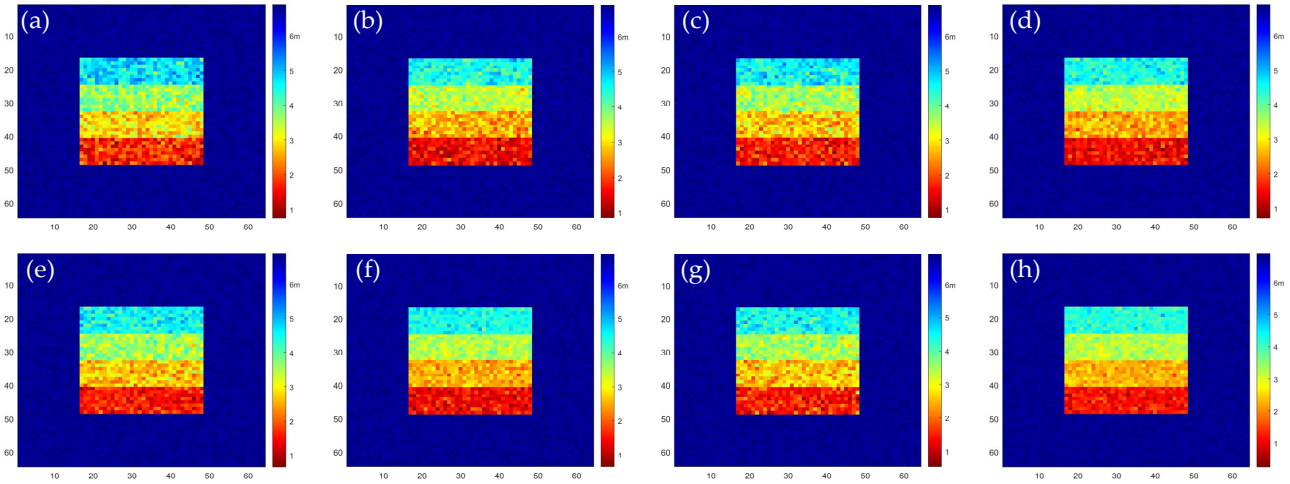


Figure 4. Reconstruction results of different fusion methods. (**a**) Equal-weight baseline; (**b**) intensity only (I-only); (**c**) uncertainty only; (**d**) polarization contrast only (Pc-only); (**e**) intensity combined with uncertainty (I + uncertainty); (**f**) intensity combined with polarization contrast (I + Pc); (**g**) polarization contrast combined with uncertainty (Pc + uncertainty); (**h**) the proposed multi-feature fusion method.

Table 3. Performance metrics of different methods in Region A.

Weight	MAE	Relative Error	MSE	RMSE	STD
Equal	0.3457	0.1383	0.2259	0.4753	0.3934
I-only	0.3155	0.1262	0.1562	0.3953	0.3056
uncertainty-only	0.3284	0.1310	0.1401	0.3743	0.3915
Pc-only	0.2963	0.1185	0.1324	0.3639	0.295
I + uncertainty	0.2899	0.1159	0.1399	0.374	0.3005
I + Pc	0.3099	0.1239	0.1485	0.3854	0.3462
Pc + uncertainty	0.2960	0.1184	0.1323	0.3638	0.2949
Multi-feature fusion method	0.2720	0.1088	0.1059	0.3255	0.2623

Table 4. Performance metrics of different methods in Region B.

Weight	MAE	Relative Error	MSE	RMSE	STD
Equal	0.3676	0.147	0.2761	0.5254	0.4439
I-only	0.3376	0.135	0.1799	0.4242	0.3639
uncertainty-only	0.3263	0.1305	0.2144	0.4630	0.3992
Pc-only	0.2835	0.1134	0.1374	0.3707	0.308
I + uncertainty	0.2904	0.1162	0.1306	0.3614	0.3063
I + Pc	0.3299	0.1319	0.1722	0.4150	0.3705
Pc + uncertainty	0.2833	0.1133	0.1375	0.3708	0.3082
Multi-feature fusion method	0.2791	0.1116	0.1208	0.3476	0.2934

Table 5. Performance metrics of different methods in Region C.

Weight	MAE	Relative Error	MSE	RMSE	STD
Equal	0.3319	0.1328	0.2348	0.4846	0.4443
I-only	0.2827	0.1131	0.1642	0.4052	0.3690
uncertainty-only	0.3199	0.1279	0.2197	0.4687	0.4201
Pc-only	0.3366	0.1346	0.1804	0.4247	0.3155
I + uncertainty	0.2471	0.0988	0.1021	0.3195	0.3085
I + Pc	0.2796	0.1118	0.1253	0.3540	0.3515
Pc + uncertainty	0.2563	0.1025	0.1060	0.3256	0.3149
Multi-feature fusion method	0.2458	0.0983	0.0900	0.3000	0.2887

Table 6. Performance metrics of different methods in Region D.

Weight	MAE	Relative Error	MSE	RMSE	STD
Equal	0.3455	0.1382	0.3311	0.0575	0.5361
I-only	0.3325	0.1330	0.3414	0.5843	0.5439
uncertainty-only	0.2925	0.1170	0.2231	0.4723	0.4487
Pc-only	0.3221	0.1288	0.2079	0.4560	0.3778
I + uncertainty	0.2176	0.0870	0.0844	0.2904	0.2845
I + Pc	0.2822	0.2822	0.1347	0.3670	0.3583
Pc + uncertainty	0.2389	0.2389	0.1067	0.3266	0.3173
Multi-feature fusion method	0.2094	0.0838	0.0690	0.2627	0.2596

In contrast, the proposed multi-feature joint weighting method achieves the best performance across all regions (A–D). In Region A, the MSE is reduced to 0.1059 from 0.2259, while the MAE, RMSE, and STD are 0.2720, 0.3255, and 0.2623, respectively. In Region B, the MSE and STD are further reduced to 0.1208 and 0.2934. In Regions C and D, the MSE is reduced to 0.0900 and 0.0690, respectively, demonstrating stronger adaptability under complex polarization scattering conditions.

The results indicate that polarization information plays an important role in regions with significant scattering variations. However, using polarization alone is still insufficient to achieve optimal performance. By fusing intensity, uncertainty, and polarization information, the proposed method provides a more comprehensive characterization of signal reliability, thereby improving reconstruction accuracy and reducing error fluctuations.

These results also show that higher Pc or higher intensity does not necessarily correspond to higher ranging accuracy, further validating the necessity of multi-feature fusion.

3.2. Robustness and Generalization Verification

To further evaluate the applicability of the proposed method in complex real-world environments, a systematic analysis is conducted from three aspects: noise level variations corresponding to different SNR conditions, imaging distance variation, and random noise perturbations. Specifically, different noise levels are simulated, resulting in varying SNR conditions, in order to reflect the impact of environmental interference and detector noise on fringe peak localization accuracy. As the noise level increases (i.e., SNR decreases), the echo signal becomes more corrupted by random fluctuations, leading to peak broadening and unstable localization, which can be interpreted as an increase in ranging uncertainty. Therefore, the variation in noise levels in this study can be regarded as an explicit representation of uncertainty under different signal quality conditions. Imaging distance variation is introduced to simulate signal attenuation and echo quality degradation in long-range detection, which affects reconstruction performance. In addition, Monte Carlo random noise perturbations are applied to evaluate the statistical stability and consistency of the method under stochastic disturbances.

Under these degradation conditions, the proposed method is compared with a non-weighted fusion baseline method. A comprehensive evaluation is performed from multiple perspectives, including robustness to noise levels, adaptability to imaging distance, and reconstruction stability, thereby providing a more complete validation of the generalization capability of the proposed method in complex practical scenarios.

3.2.1. Simulation Procedure and Experimental Setup

Based on the four-layer step target model described above, comparative experiments under different noise levels are conducted. The target structure, material parameters, and imaging pipeline are kept unchanged. The imaging distance is fixed at 1000 m. Three noise levels corresponding to SNR settings of 5 dB, 10 dB, and 15 dB are considered.

Under each noise condition, both the non-weighted reconstruction method and the proposed multi-feature weighted reconstruction method are applied to fuse the three single-wavelength depth images. Two sets of reconstructed depth images are then obtained for performance comparison under different noise levels. The depth reconstruction results are shown in Figure 5.

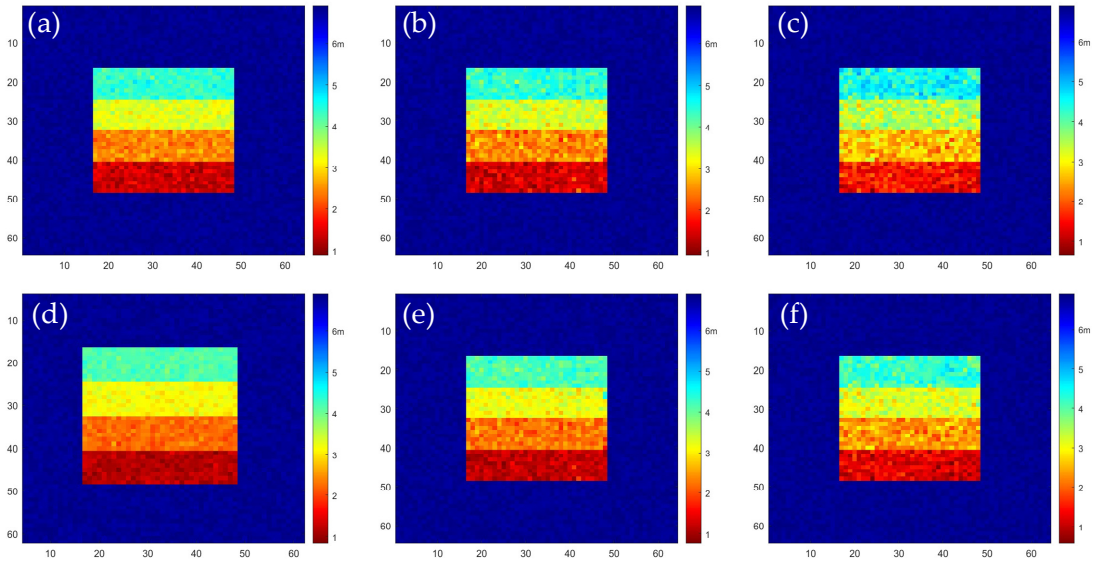


Figure 5. Depth reconstruction results under different noise levels. (**a**–**c**) Equal method at 15, 10, and 5 dB, respectively; (**d**–**f**) multi-feature fusion method at 15, 10, and 5 dB, respectively.

As can be observed from the figure, under low SNR conditions (e.g., 5 dB), increased noise levels significantly affect the depth reconstruction results. The non-weighted method exhibits obvious depth fluctuations and structural distortions, whereas the proposed method can effectively suppress noise interference to a certain extent and maintain a relatively clear step structure. As the noise level decreases (corresponding to higher SNR conditions), the reconstruction results of all methods improve gradually. The proposed method consistently demonstrates better structural preservation capability and lower sensitivity to noise under different noise conditions.

For quantitative analysis, the mean depth values of the four step regions are calculated, and evaluation metrics including Mean Absolute Error (MAE), Relative Error (RE), Mean Squared Error (MSE), Root Mean Square Error (RMSE), and Standard Deviation (STD) are further computed. A comparative evaluation of the two methods is performed under different noise levels corresponding to SNR conditions.

The evaluation results of different regions are presented in Tables 7–10.

Table 7. Error metrics of Region A under different noise levels.

	Noise Level (SNR Condition)	MAE	Relative Error	MSE	RMSE	STD
Without weighting	15 dB	0.1868	0.0441	0.0461	0.2147	0.1558
	10 dB	0.2594	0.0648	0.1019	0.3193	0.2493
	5 dB	0.3786	0.0946	0.2695	0.5191	0.5168
Weighted reconstruction	15 dB	0.1727	0.0432	0.0443	0.2106	0.1470
	10 dB	0.2290	0.0573	0.0818	0.2860	0.2105
	5 dB	0.3040	0.0760	0.1422	0.3771	0.3174

Table 8. Error metrics of Region B under different noise levels.

	Noise Level (SNR Condition)	MAE	Relative Error	MSE	RMSE	STD
Without weighting	15 dB	0.1960	0.0697	0.0499	0.2235	0.1504
	10 dB	0.2345	0.0782	0.0842	0.2902	0.2388
	5 dB	0.3891	0.1297	0.2585	0.5084	0.4465
Weighted reconstruction	15 dB	0.1821	0.0607	0.0472	0.2172	0.1426
	10 dB	0.2170	0.0723	0.0743	0.2725	0.2270
	5 dB	0.3050	0.1017	0.1383	0.3718	0.3137

Table 9. Error metrics of Region C under different noise levels.

	Noise Level (SNR Condition)	MAE	Relative Error	MSE	RMSE	STD
Without weighting	15 dB	0.1473	0.0792	0.0284	0.1686	0.1698
	10 dB	0.2365	0.1183	0.0818	0.2860	0.2696
	5 dB	0.3821	0.1911	0.2672	0.5169	0.5112
Weighted reconstruction	15 dB	0.1358	0.0679	0.0277	0.1663	0.1654
	10 dB	0.2008	0.1004	0.0608	0.2466	0.2305
	5 dB	0.2499	0.1250	0.0974	0.3121	0.3005

Table 10. Error metrics of Region D under different noise levels.

	Noise Level (SNR Condition)	MAE	Relative Error	MSE	RMSE	STD
Without weighting	15 dB	0.1370	0.1370	0.0293	0.1711	0.1644
	10 dB	0.2306	0.2306	0.1081	0.3287	0.3145
	5 dB	0.3863	0.3863	0.3961	0.6293	0.5973
Weighted reconstruction	15 dB	0.1203	0.1203	0.0233	0.1527	0.1500
	10 dB	0.1978	0.1978	0.0602	0.2454	0.2373
	5 dB	0.2572	0.2572	0.1074	0.3278	0.3190

The results in Tables 7–10 indicate that, as the noise level increases (corresponding to decreasing SNR conditions from 15 dB to 5 dB), the error metrics of all methods show a significant increasing trend, suggesting that noise interference directly affects the accuracy of fringe peak localization, thereby degrading depth reconstruction performance.

Compared with the non-weighted method, the proposed multi-feature joint weighting method consistently achieves lower MSE and RMSE under all noise conditions, and also exhibits smaller STD values. In particular, under low signal-to-noise conditions (5 dB, corresponding to higher noise levels), the proposed method can still effectively preserve the integrity of the step structure and suppress depth fluctuations caused by noise. These results indicate that the proposed multi-feature joint weighting strategy can more comprehensively characterize signal quality, thereby significantly improving robustness to noise and overall system stability.

3.2.2. Experiments Under Different Imaging Distances

To validate the applicability of the proposed method under different detection distances, robustness experiments are conducted based on the four-layer step target model described above. During the experiments, the target structure, material parameters, wavelength settings, and data processing pipeline are kept unchanged. The noise level is fixed (corresponding to a signal-to-noise ratio of 15 dB) to eliminate the influence of noise variations, with a focus on analyzing the effect of imaging distance on depth reconstruction performance.

Specifically, three distances—500 m, 1000 m, and 1500 m—are set. Under each distance condition, both the non-weighted fusion method and the proposed multi-feature joint weighting method are applied to fuse and reconstruct the three single-wavelength depth images, thereby obtaining the depth reconstruction results under different distance conditions. The resulting depth images are shown in Figure 6.

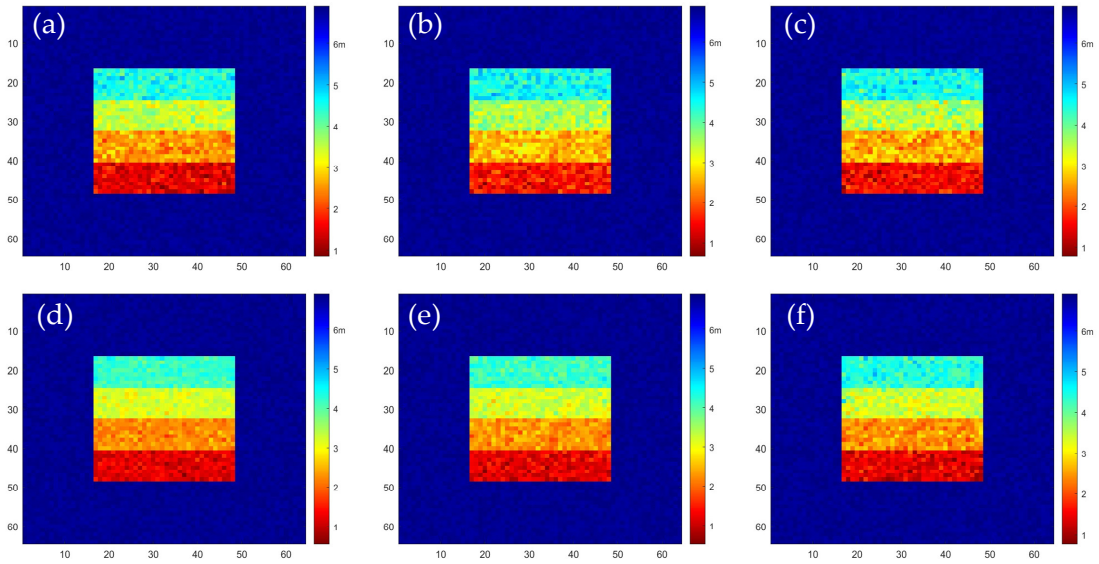


Figure 6. Shows the depth reconstruction results under different imaging distances. (**a**–**c**) Equal method at 500, 1000, and 1500 m, respectively; (**d**–**f**) multi-feature fusion method at 500, 1000, and 1500 m, respectively.

As shown in Figure 6, as the imaging distance increases, the echo signal intensity gradually decreases, and the effects of noise interference and peak localization errors on depth reconstruction become more pronounced. The non-weighted method exhibits local depth fluctuations under long-distance conditions, whereas the proposed method can better preserve the integrity of the step structure and effectively reduce reconstruction errors caused by increasing distance.

For quantitative evaluation, the mean depth values of the four step regions are computed, and several metrics, including Mean Absolute Error (MAE), Relative Error (RE), Mean Squared Error (MSE), Root Mean Square Error (RMSE), and Standard Deviation (STD), are further calculated. A comparative analysis of the two methods is then performed under different distance conditions.

The evaluation results of different regions are presented in Tables 11–14.

The results in Tables 11–14 indicate that, as the imaging distance increases from 500 m to 1500 m, the error metrics of all methods exhibit an overall increasing trend. This is mainly attributed to the attenuation of the echo signal caused by the increased propagation distance, which further aggravates the error in streak peak extraction.

Table 11. Error metrics of Region A under different distances.

Method	Distance	MAE	Relative Error	MSE	RMSE	STD
Without weighting	500 m	0.2526	0.0631	0.1180	0.3435	0.2707
	1000 m	0.2700	0.0675	0.1248	0.3533	0.2745
	1500 m	0.2908	0.0727	0.1391	0.3729	0.3359
Weighted reconstruction	500 m	0.2301	0.0575	0.0786	0.2804	0.2158
	1000 m	0.2320	0.0580	0.0823	0.2868	0.2180
	1500 m	0.2371	0.0593	0.0883	0.2971	0.2350

Table 12. Error metrics of Region B under different distances.

Method	Distance	MAE	Relative Error	MSE	RMSE	STD
Without weighting	500 m	0.2414	0.0805	0.0897	0.2996	0.2251
	1000 m	0.2606	0.0869	0.0998	0.3159	0.2548
	1500 m	0.2866	0.0955	0.1343	0.3664	0.3108
Weighted reconstruction	500 m	0.2293	0.0754	0.0816	0.2856	0.2148
	1000 m	0.2302	0.0767	0.0829	0.2880	0.2283
	1500 m	0.2328	0.0776	0.0882	0.2969	0.2564

Table 13. Error metrics of Region C under different distances.

Method	Distance	MAE	Relative Error	MSE	RMSE	STD
Without weighting	500 m	0.2210	0.1105	0.0884	0.2974	0.2635
	1000 m	0.2566	0.1283	0.1044	0.3231	0.2857
	1500 m	0.3079	0.1540	0.1400	0.3742	0.3150
Weighted reconstruction	500 m	0.1731	0.0865	0.0497	0.2229	0.2184
	1000 m	0.1836	0.0918	0.0557	0.2360	0.2262
	1500 m	0.1884	0.0942	0.0589	0.2427	0.2382

Table 14. Error metrics of Region D under different distances.

Method	Distance	MAE	Relative Error	MSE	RMSE	STD
Without weighting	500 m	0.2156	0.2156	0.0689	0.2625	0.2618
	1000 m	0.2525	0.2525	0.0972	0.3117	0.2984
	1500 m	0.2954	0.2954	0.1569	0.3962	0.3136
Weighted reconstruction	500 m	0.1808	0.1808	0.0507	0.2253	0.2228
	1000 m	0.1823	0.1823	0.0520	0.2281	0.2237
	1500 m	0.1888	0.1888	0.0571	0.2389	0.2348

In contrast, the proposed multi-feature joint weighting method consistently maintains lower MSE and RMSE values under different distance conditions, and its error growth rate is smaller than that of the non-weighted method. In particular, under long-distance conditions (1500 m), the proposed method can still effectively preserve the structural hierarchy of the step target, demonstrating stronger adaptability to signal attenuation.

These results indicate that the proposed method not only achieves high accuracy in short- and medium-range scenarios, but also maintains effective error control in long-distance detection, thereby demonstrating excellent distance robustness.

3.2.3. Monte Carlo Repeated Experiments

To further evaluate the stability and consistency of the proposed method under random noise perturbations, Monte Carlo repeated experiments are conducted under fixed experimental conditions. The experiments are still based on the four-layer step target model described above, with unchanged target structure, material parameters, and imaging pipeline. The noise level is fixed, corresponding to a SNR of 10 dB, and the imaging distance is fixed at 1000 m.

Under this condition, 20 independent repeated experiments are conducted for both the unweighted fusion method and the proposed multi-feature joint weighting method. In each experiment, random noise is regenerated and the complete depth reconstruction process is performed to obtain reconstruction results under different noise conditions. For each experiment, the reconstruction results are evaluated using mean absolute error

(MAE), relative error (RE), mean squared error (MSE), root mean square error (RMSE), and standard deviation (STD). The mean and variance of these metrics are then calculated to assess the stability of different methods under random noise perturbations. The results are shown in Table 15.

Table 15. Comparison of reconstruction performance between the proposed method and the unweighted method.

Region	Method	MAE	Relative Error	MSE	RMSE	STD
A	Proposed	0.2331 ± 0.0102	0.0583 ± 0.0025	0.0814 ± 0.0068	0.2850 ± 0.0119	0.2246 ± 0.0079
	Unweighted	0.2576 ± 0.0104	0.0651 ± 0.0027	0.1025 ± 0.0072	0.3192 ± 0.0098	0.2529 ± 0.0088
B	Proposed	0.2385 ± 0.0113	0.0795 ± 0.0038	0.0849 ± 0.0089	0.2911 ± 0.0152	0.2235 ± 0.0105
	Unweighted	0.2570 ± 0.0125	0.0846 ± 0.0037	0.1028 ± 0.0105	0.3205 ± 0.0165	0.2622 ± 0.0193
C	Proposed	0.1836 ± 0.0097	0.0918 ± 0.0049	0.0529 ± 0.0065	0.2298 ± 0.0141	0.2214 ± 0.0118
	Unweighted	0.2137 ± 0.0155	0.1064 ± 0.0077	0.0784 ± 0.0210	0.2716 ± 0.0365	0.2663 ± 0.0348
D	Proposed	0.1860 ± 0.0085	0.1860 ± 0.0085	0.0542 ± 0.0072	0.2328 ± 0.0156	0.2224 ± 0.0129
	Unweighted	0.2163 ± 0.0123	0.2163 ± 0.0123	0.0830 ± 0.0295	0.2920 ± 0.0502	0.2751 ± 0.0418

The results in Table 15 indicate that, under the condition of 15 dB noise perturbation, the proposed method outperforms the unweighted method across all four regions (A, B, C, and D), demonstrating improved reconstruction stability and robustness to stochastic noise.

Overall, the proposed method achieves average MAE, RE, MSE, RMSE, and STD values of 0.2103, 0.1039, 0.0684, 0.2597, and 0.2230, respectively, which are all lower than those of the non-weighted method (0.2362, 0.1181, 0.0917, 0.3008, and 0.2641). The corresponding average reductions are approximately 10.95%, 12.02%, 25.44%, 13.68%, and 15.58%, respectively.

These results demonstrate that the proposed multi-feature joint weighting method not only improves reconstruction accuracy but also enhances consistency under random noise perturbations, further validating its robustness.

A comprehensive evaluation under varying noise levels (corresponding to different SNR conditions), imaging distances, and stochastic perturbations shows that the error of all methods increases with stronger noise or longer propagation distance. However, the proposed method consistently maintains lower error levels and reduced fluctuations. In particular, under low signal-to-noise conditions (5 dB) and long-distance scenarios (1500 m), the proposed method still effectively preserves the structural integrity of the target, demonstrating strong robustness to noise and good adaptability to distance variation.

Monte Carlo repeated experiments further confirm that the proposed method achieves lower reconstruction error under multiple random perturbations, with an average error reduction of approximately 10–25%, validating its stability and consistency.

Overall, the proposed method demonstrates clear advantages in terms of accuracy, robustness, and generalization capability.

3.3. Contrast Experiment

To validate the proposed method for contrast enhancement in complex scenes, multispectral polarization imaging simulations are conducted based on the MSP-STIL imaging system. In this experiment, the target is partially occluded by trees, forming a low-contrast scene with strong background interference.

After obtaining multi-wavelength echo signals, intensity images, Pc images, and depth images are reconstructed. To eliminate amplitude differences among different channels, all images are normalized prior to fusion processing.

From the seven reconstructed images, three representative images are selected based on complementary feature characteristics for fusion analysis. These selected images are mapped to the RGB channels to construct a fused RGB image.

Subsequently, the RGB fused image is compared with intensity images, polarization images, and depth images for contrast analysis. A contrast evaluation metric (CST) is adopted for quantitative assessment of different image types. In addition, the RGB image is converted into the HSV (Hue, Saturation, Value) color space for further contrast computation. The contrast calculation method is given as follows:

$$CST = \sum_{c=1}^{c_n} \left| \frac{\frac{1}{K_c}\sum Target_c(k) - \frac{1}{M_c}\sum Background_c(m)}{\frac{1}{M_c}\sum Background_c(m)} \right| \quad (25)$$

where c_n denotes the number of image channels. Specifically, $c_n = 1$ corresponds to a single-channel image, and $c_n = 3$ corresponds to an HSV image. $target_c(k)$ represents the pixel value of the target in channel c; K_c is the total number of target pixels in channel c. $background_c(m)$ denotes the pixel value of the background in channel c; and M_c is the total number of background pixels in channel c. In the contrast evaluation process, the target and background regions are determined through manual annotation.

As shown in the figures above, Figure 7 presents the reflectance images of the target region at three wavelengths. Figure 8 shows the m_{11} component of the Mueller matrix for the target region at the three wavelengths, while Figure 9 shows the m33 component. Figure 10 displays the original distance image of the target region, in which the tank is partially occluded by three trees.

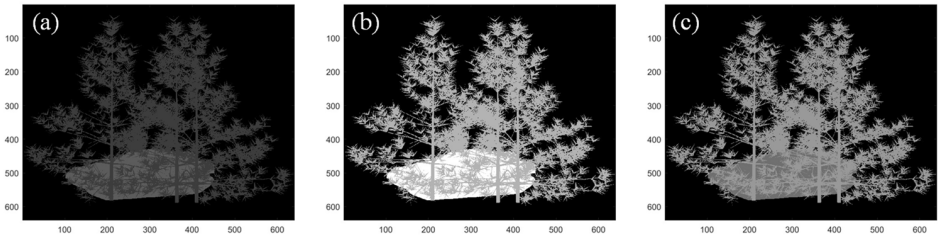


Figure 7. Reflectance images: (**a**) reflectance image at λ_1; (**b**) reflectance image at λ_2; (**c**) reflectance image at λ_3.

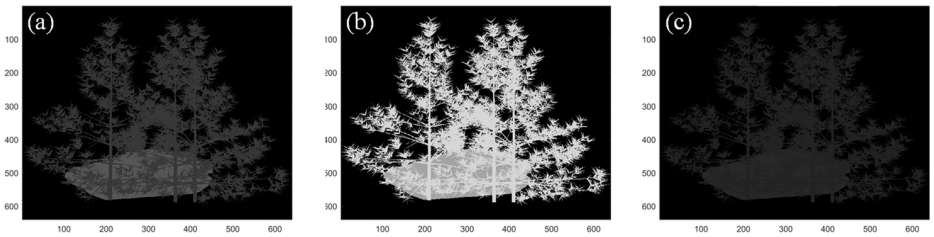


Figure 8. m_{11} images: (**a**) m_{11} image at λ_1; (**b**) m_{11} image at λ_2; (**c**) m_{11} image at λ_3.

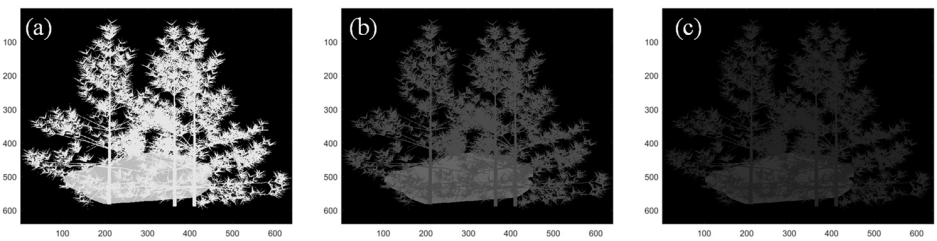


Figure 9. m_{33} images: (**a**) m_{33} image at λ_1; (**b**) m_{33} image at λ_2; (**c**) m_{33} image at λ_3.

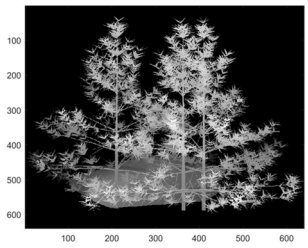


Figure 10. Initial depth image.

From Figure 11, it is observed that in single-wavelength images, the brightness distribution of the target tank is similar to that of the occluding trees. Alternatively, due to the relatively low reflectance of the tank, its brightness appears darker. As a result, the overall image contrast is low and the target features are not prominent, thereby increasing the difficulty of target recognition. Table 16 shows the CST of each single-wavelength image and depth map.

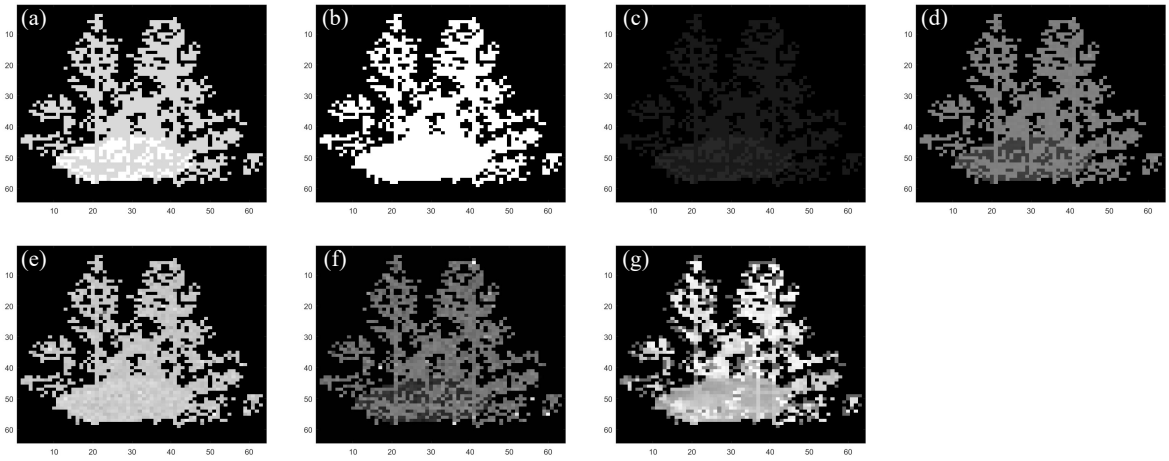


Figure 11. Reconstructed intensity images, DOP images and the depth image. (**a**) Intensity image at λ_1. (**b**) Intensity image at λ_2. (**c**) Intensity image at λ_3. (**d**) DOP image at λ_1. (**e**) DOP image at λ_2. (**f**) DOP image at λ_3. (**g**) Depth image.

Table 16. Comparison of CST metrics for different image types.

Image Type	CST
Pc image (λ_1)	0.7949
Pc image (λ_2)	0.1563
Pc image (λ_3)	0.5203
Intensity image (λ_1)	0.5121
Intensity image (λ_2)	0.0585
Intensity image (λ_3)	0.3260
Fused depth image	0.0217

On this basis, all seven images are exhaustively combined using permutation-based selection, and each three-image subset is mapped to the RGB channels to construct all possible three-channel fusion schemes. Since the channel assignment is order-sensitive (i.e., different permutations of R, G, and B lead to different fused results), a total of 210 distinct RGB fusion combinations are generated, corresponding to the permutation of selecting 3 images from 7 channels (i.e., P(7,3) = 210).

For each fusion result, the image contrast metric (CST) is calculated, and a unified statistical analysis is performed over all combinations. Figure 12 shows the contrast ranking

curve of the 210 fusion results, which provides an intuitive representation of the overall contrast distribution among different combinations.

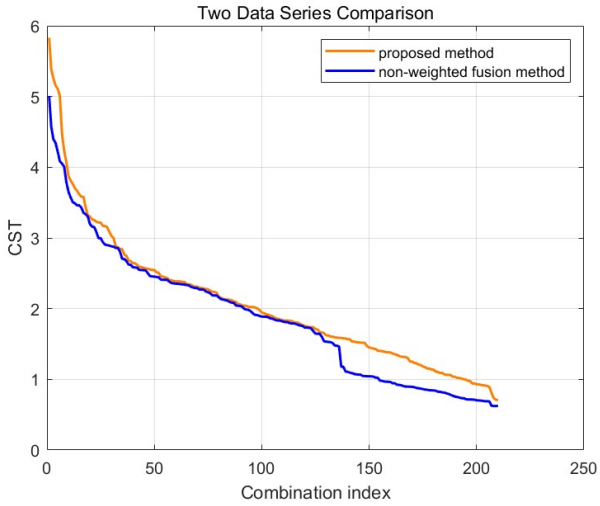


Figure 12. Contrast ranking curve of 210 fusion results.

On this basis, the top three combinations with the highest contrast are selected for visualization. Figure 13a–c show the three best fusion results obtained by the non-weighted fusion method, while (d–f) show the corresponding results of the proposed method.

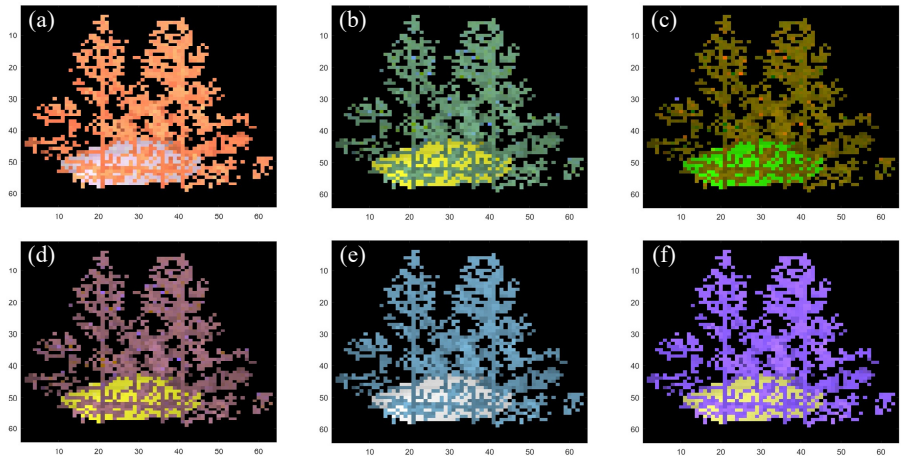


Figure 13. RGB images of the best fusion results obtained by the non-weighted method and the proposed method. (**a**–**c**) RGB images of the three best fusion results obtained by the non-weighted method. (**d**–**f**) Corresponding RGB images of the three best fusion results achieved by the proposed method.

The experimental results show that the optimized method significantly outperforms the original method in terms of overall contrast distribution. It not only achieves a higher maximum contrast but also maintains a consistently higher contrast level across the entire distribution range. This indicates that the improved method can stably enhance image contrast.

These results further demonstrate that the proposed method effectively improves the representation capability of multimodal information and exhibits strong statistical stability and generalization ability.

Experimental results demonstrate that the overall contrast of single-wavelength images is relatively low. As shown in Table 16, the CST values of Pc images are 0.7949, 0.1563, and 0.5203, while those of intensity images are 0.5121, 0.0585, and 0.3260. The fused depth

image yields a CST value of only 0.0217, indicating that single-modality images have clear limitations in distinguishing targets from background.

Through multimodal RGB fusion, the image contrast is significantly improved. As shown in Table 17, the CST range of the original method is 0.6227–5.0065, while that of the optimized method increases to 0.7063–5.8300, corresponding to an approximate 16.5% improvement in maximum contrast. Compared with the maximum value of single-modality images (0.7949), the fusion results achieve a substantial enhancement.

Table 17. Comparison of RGB image contrast before and after reconstruction method optimization.

Image Type	CST
RGB fused image (before optimization)	0.6227–5.0065
RGB fused image (after optimization)	0.7063–5.8300

In addition, statistical analysis of the 210 fusion combinations shows that the contrast distribution curve of the optimized method shifts upward across the entire range, indicating not only improved optimal performance but also enhanced overall stability, which reflects good robustness and generalization ability.

Overall, the proposed method significantly enhances image contrast in occluded and low-reflectivity complex scenes. By fusing intensity, polarization, and depth information, it effectively compensates for the limitations of single-modality representations and significantly improves target discriminability.

Meanwhile, the improvement in the overall contrast distribution indicates that the method not only achieves higher peak performance but also exhibits strong stability and generalization capability, providing a more reliable image basis for subsequent target detection and recognition.

4. Conclusions

This paper addresses the limitations of conventional streak tube imaging LiDAR (STIL) in complex scattering environments, including weak echo detection, low target–background contrast, and unstable multi-dimensional fusion. A multispectral polarization fusion (MSP-STIL) fringe reconstruction method is proposed. By constructing a multi-wavelength polarization-modulated imaging system and introducing adaptive fusion with multi-feature weighting, joint modeling of intensity, polarization, and noise-induced uncertainty is achieved, improving reconstruction accuracy and robustness.

A multispectral STIL system is developed, enabling simultaneous emission at 355 nm, 532 nm, and 1064 nm with polarization modulation. Multi-channel echo signals are temporally mapped and reconstructed in the streak imaging process. An adaptive Pc-based mechanism is introduced to enhance fringe stability under weak echo conditions.

In reconstruction, a multi-feature joint weighting strategy is proposed, integrating intensity, Pc, peak width, and uncertainty-related noise characteristics into an adaptive fusion model. The method can be interpreted as an uncertainty-driven inverse-variance-like fusion strategy, enabling adaptive channel weighting under varying noise and scattering conditions.

Extensive simulations based on a four-step target evaluate performance under fusion strategies, noise variation, imaging distance, and stochastic perturbations. Results show:

(1) The proposed method achieves the best reconstruction accuracy across all regions, with MSE reduced to 0.0690 and significant reductions in RMSE and STD, indicating improved stability;
(2) Under low signal-to-noise conditions (5 dB), it maintains clear structure and superior robustness compared to the non-weighted method;

(3) Across 500–1500 m imaging distances, it shows stable error growth and good long-range adaptability;
(4) In contrast evaluation, multispectral RGB fusion improves CST significantly, with the proposed method achieving 0.7063–5.8300 compared to 0.6227–5.0065 for the baseline, with up to 16.5% improvement.

Overall, the proposed method enhances STIL performance in terms of accuracy, robustness, and generalization by integrating multispectral and polarization information with an uncertainty-aware adaptive weighting mechanism.

In the conclusion, we further note that future work will first conduct systematic experiments under varying materials, occlusion levels, and incident angles to validate the generalization capability of the proposed method. In addition, metrics such as contrast-to-noise ratio (CNR), probability of detection, false alarm rate, and ROC/AUC will be introduced for a more comprehensive evaluation from the perspective of target detection and recognition. Finally, future efforts will focus on real-world optical system experiments and practical validation, together with more advanced atmospheric scattering models and deep learning-based adaptive fusion strategies for hardware implementation, to enhance the reliability and applicability of the method.

Author Contributions: Conceptualization: Y.Z. and S.G.; methodology: Y.Z., S.X. and W.L.; validation: W.L., X.L. (Xiuli Luo), and S.X.; formal analysis: Y.Z. and X.L. (Xuan Li); investigation: Y.Z., S.X., W.L. and X.L. (Xiuli Luo); resources: L.W. and S.G.; data curation: Y.Z. and S.X.; writing—original draft: Y.Z.; writing—review and editing: Y.Z., S.X., W.L., X.L. (Xuan Li), X.L. (Xiuli Luo), S.G. and L.W.; visualization: Y.Z. and S.X.; supervision: S.G.; project administration: S.G.; funding acquisition: S.G. All authors have read and agreed to the published version of the manuscript.

Funding: This research was supported by the Fundamental Research Program of Shanxi Province, grant number: 202303021212207.

Data Availability Statement: The data presented in this study are available upon request from the corresponding author.

Conflicts of Interest: The authors declare no conflicts of interest.

References

1. Gao, J.; Zhang, H.; Sun, J.; Wang, Q. A Three-Dimensional High-Resolution Imaging Method for Multi-Slit Streak Tube Based on Compressed Sensing. In *Proceedings of the 2024 IEEE Academic International Conference*; IEEE: Piscataway, NJ, USA, 2024; pp. 101–105.
2. Clermont, L.; Uhring, W.; Georges, M. Stray light characterization with ultrafast time-of-flight imaging. *Sci. Rep.* **2021**, *11*, 10081. [CrossRef] [PubMed]
3. Chen, J.; Li, H.; Zhan, W.; Dong, Y.; Wu, L.; Wang, W. Simulation and Analysis of Coherent Wind Lidar Based on Range Resolution. *Sensors* **2025**, *25*, 2344. [CrossRef] [PubMed]
4. Morsy, A.; Kuijk, M. Correlation-Assisted Pixel Array for Direct Time of Flight. *Sensors* **2024**, *24*, 5380. [CrossRef] [PubMed]
5. Farooq, A.; Alquaity, A.B.S.; Raza, M.; Nasir, E.F.; Yao, S.; Ren, W. Laser sensors for energy systems and process industries: Perspectives and directions. *Prog. Energy Combust. Sci.* **2022**, *91*, 100997. [CrossRef]
6. Wolf, A.; Dostovalov, A.; Bronnikov, K.; Skvortsov, M.; Wabnitz, S.; Babin, S. Advances in femtosecond laser direct writing of fiber Bragg gratings in multicore fibers: Technology, sensor and laser applications. *Opto-Electron. Adv.* **2022**, *5*, 210055. [CrossRef]
7. Bai, Z.; Zhao, Z.; Tian, M.; Jin, D.; Pang, Y.; Li, S.; Yan, X.; Wang, Y.; Lu, Z. A comprehensive review on the development and applications of narrow-linewidth lasers. *Microw. Opt. Technol. Lett.* **2022**, *64*, 2244–2255.
8. Zhu, G.; Xu, Z.; Jin, Y.; Chen, X.; Yang, L.; Xu, J.; Shan, D.; Chen, Y.; Guo, B. Mechanism and application of laser cleaning: A review. *Opt. Lasers Eng.* **2022**, *157*, 107130. [CrossRef]
9. Zhai, Y.; Zhang, Z.; Xie, S.; Tong, C.; Wang, L. Simulation Algorithm for Depth Images of Imaging LiDAR. In *Proceedings of the 2025 5th International Conference on Imaging LiDAR*; IEEE: Piscataway, NJ, USA, 2025; pp. 214–218.

10. Dong, C.; Fan, R.; Fan, Z.; Chen, Z.; Dong, Z.; Chen, D. Research of the Richardson-Lucy Algorithm Based Deblurring Method for Enhancing Spatial Resolution in Streak-Tube Imaging Lidar. In *Proceedings of the 2024 IEEE Academic International Conference*; IEEE: Piscataway, NJ, USA, 2024; pp. 212–215.
11. Chu, Y.; Cao, J.; Ding, W.; Huang, J.; Ju, H.; Cao, H.; Liu, G. Hyperspectral image classification using feature fusion fuzzy graph broad network. *Inf. Sci.* **2025**, *689*, 121504. [CrossRef]
12. Zhang, Z.; Yang, Z.; Li, G.; Chen, D.; Wang, X. Analysis of influence factors of target polarization characteristics. *Sci. Rep.* **2023**, *13*, 21784. [CrossRef] [PubMed]
13. Liu, J.; Xu, R.; Duan, Y.; Guo, T.; Shi, G.; Luo, F. MDGF-CD: Land-cover change detection with multi-level DiffFormer feature grouping fusion for VHR remote sensing images. *Inf. Fusion* **2025**, *120*, 103110. [CrossRef]
14. Guo, S.; Li, W.; Lai, Z.; Meng, X.; Han, S.; Zhai, Y. Design and modeling of multi-spectral polarimetry streak tube imaging LiDAR. *Infrared Phys. Technol.* **2021**, *118*, 103872. [CrossRef]
15. Zhou, J.; Zhou, Y.; Ni, X.; Wang, F.; Ying, X.; Huang, M.; Xu, Z.; Chen, F.; Liu, Y.; Chen, J. Research progress and applications of polarization integrated infrared photodetector. *Opto-Electron. Eng.* **2023**, *50*, 230010. (In Chinese)
16. Zhang, Y.; Wu, T.; Zhang, X.; Sun, Y.; Wang, Y.; Li, S.; Li, X.; Zhao, K.; Yan, Z.; Xu, D.; et al. Rayleigh Lidar Signal Denoising Method Combined with WT, EEMD and LOWESS to Improve Retrieval Accuracy. *Remote Sens.* **2022**, *14*, 3270. [CrossRef]
17. Cheng, Z.; Li, Z.; She, W.; Xia, A. Compound denoising method of laser speckle noise in laser inherent field imaging. *Acta Phys. Sin.* **2019**, *68*, 054206. (In Chinese) [CrossRef]
18. Yue, Z.; Ruan, P.; Fang, M.; Chen, P.; Wang, X.; Xie, Y.; Xie, M.; Hao, W.; Chen, S. Restoration of Streak Tube Imaging LiDAR 3D Images in Photon Starved Regime Using Multi-Sparsity Constraints and Adaptive Regularization. *Remote Sens.* **2025**, *17*, 3089. [CrossRef]
19. Zhang, M.; Li, Z.; Zhang, F.; Ma, L. Adaptive Bidirectional Gray-Scale Center of Gravity Extraction Algorithm of Laser Stripes. *Sensors* **2022**, *22*, 9567. [CrossRef] [PubMed]

Disclaimer/Publisher's Note: The statements, opinions and data contained in all publications are solely those of the individual author(s) and contributor(s) and not of MDPI and/or the editor(s). MDPI and/or the editor(s) disclaim responsibility for any injury to people or property resulting from any ideas, methods, instructions or products referred to in the content.